



**AALBORG UNIVERSITY**  
DENMARK

**Aalborg Universitet**

## **Measurement-Based Channel Characterization in a Large Hall Scenario at 300 GHz**

Lyu, Yejian; Yuan, Zhiqiang; Gao, Huaqiang; Zhu, Qiuming; Zhang, Xiang; Fan, Wei

*Published in:*  
China Communications

*DOI (link to publication from Publisher):*  
[10.23919/JCC.fa.2022-0286.202304](https://doi.org/10.23919/JCC.fa.2022-0286.202304)

*Creative Commons License*  
CC BY 4.0

*Publication date:*  
2023

*Document Version*  
Accepted author manuscript, peer reviewed version

[Link to publication from Aalborg University](#)

*Citation for published version (APA):*  
Lyu, Y., Yuan, Z., Gao, H., Zhu, Q., Zhang, X., & Fan, W. (2023). Measurement-Based Channel Characterization in a Large Hall Scenario at 300 GHz. *China Communications*, 20(4), 118-131. <https://doi.org/10.23919/JCC.fa.2022-0286.202304>

### **General rights**

Copyright and moral rights for the publications made accessible in the public portal are retained by the authors and/or other copyright owners and it is a condition of accessing publications that users recognise and abide by the legal requirements associated with these rights.

- Users may download and print one copy of any publication from the public portal for the purpose of private study or research.
- You may not further distribute the material or use it for any profit-making activity or commercial gain
- You may freely distribute the URL identifying the publication in the public portal -

### **Take down policy**

If you believe that this document breaches copyright please contact us at [vbn@aub.aau.dk](mailto:vbn@aub.aau.dk) providing details, and we will remove access to the work immediately and investigate your claim.

# Measurement-Based Channel Characterization in a Large Hall Scenario at 300 GHz

Yejian Lyu, Zhiqiang Yuan, Huaqiang Gao, Qiuming Zhu, Xiang Zhang, and Wei Fan

**Abstract**—Sub-terahertz (Sub-THz), defined as the frequency bands in 100-300 GHz, is promising for future generation communications and sensing applications. Accurate channel measurement and modeling are essential for development and performance evaluation of the future communication systems. Accurate channel modeling relies on realistic channel data, which should be collected by high-fidelity channel sounder. This paper presents the measurement-based channel characterization in a large indoor scenario at 299-301 GHz. We firstly review the state-of-the-art channel measurements at sub-THz frequency bands. We then presented a VNA-based channel sounder for long-range measurements, which uses the radio-over-fiber techniques. Channel measurements using this channel sounder are conducted in a large hall scenario. Based on the measurement data, we calculated and analyzed key propagation channel parameters, e.g., path loss, delay spread, and angular spread. The results are also analyzed both in the line-of-sight (LoS) and none-LoS (NLoS) cases. The large delay components in the measurements demonstrate the possibility of the long-range channel measurement campaign at 300 GHz.

**Index Terms**—Channel measurement; Sub-Terahertz; 300 GHz; Channel characterization.

## I. INTRODUCTION

Future wireless communication systems, i.e., beyond fifth-generation (B5G), are attracting increasing attention worldwide as the demand for high data-rate in various applications continue to grow rapidly [1]–[3]. Sub-terahertz (sub-THz) technologies, which is defined as the frequency bands in 100-300 GHz, are foreseen to be one of the core radio technologies for B5G communication systems, due to their large unused and untapped frequency resource [4]–[7]. Sub-THz frequency bands can potentially support the opportunity for high data-rate. Nonetheless, this frequency band still faces many challenges. As demonstrated in [4], compared to the atmospheric attenuation at lower frequency bands, the atmospheric attenuation at sub-THz bands is much higher. Moreover, with the frequency goes higher, the wavelength of the sub-THz frequencies is close to the size of dust and rain, which makes the channel at sub-THz bands behave differently than the conventional low frequency spectrum [8].

Y. Lyu, H. Gao, and W. Fan are with the Antennas, Propagation and Millimetre-Wave Systems (APMS) Section, Aalborg University, Aalborg 9220, Denmark.

Z. Yuan is with Beijing University of Posts and Telecommunications, Beijing 100876, China, and Aalborg University.

Qiuming Zhu is with Key Laboratory of Dynamic Cognitive System of Electromagnetic Spectrum Space, College of Electronic and Information Engineering, Nanjing University of Aeronautics and Astronautics, Nanjing 211106, China.

Xiang Zhang is with China Academy of Information and Telecommunications Technology (CAICT), Beijing 100191, China

(Corresponding author: Wei Fan. E-mail: wfa@es.aau.dk)

The channel sounder is essential for recording reliable channel data in the channel measurements. We can classify the channel sounding systems presented in the literature into two types based on the channel sounding technologies, one is the time-domain channel sounders such as correlation-based sounder, and the other is the frequency-domain channel sounders. The vector network analyzer (VNA) is a widely used scheme for the frequency-domain sounder, since it offers many unique advantages, e.g., scalable operating bandwidth and easy calibration [9], [10]. Since the signal generator and analyzer are co-located in the VNA, the VNA requires cable connections to remote the antennas. However, the power loss through the coaxial cable increases with the frequency. Consequently, the reduced dynamic range results in the limited measurement range, especially at sub-THz bands. To address this issue, since the optical fiber cables has a low signal loss, radio-over-fiber (RoF) techniques are employed in VNA-based sounders, which uses an electrical-to-optical unit (i.e., laser) to modulate an electrical signal to optical, transmits the signal through an optical fiber cable, and demodulates the signal into electrical by an optical-to-electrical unit i.e., photo detector) [11].

Numerous sub-THz measurement campaigns have been proposed in the recent literature. We can group the channel measurements into two categories in terms of the measurement distance and the size of the measurement scenarios, i.e., short-range measurements and long-range measurements. The high propagation loss at sub-THz bands and the hardware limitations limit the use of the sub-THz channel sounder. Therefore, many researchers are focusing on sub-THz channel in the short-range indoor scenarios, e.g., office and meeting room [7], [12]–[18]. Ultrawideband 300 GHz channel measurements in an indoor office room scenario were presented in [12], where key channel parameters, e.g., delay spreads and  $K$ -factors were analyzed. Channel measurements and comparison at three frequency bands, i.e., 10 GHz, 60 GHz, and 300 GHz, were carried out in [13] in an office room scenario, where the channel sounder was based on the correlation. The results illustrated the frequency-dependence of the multipath richness, and the 300 GHz multipath richness of the radio channel is much less than that at 60 GHz. The channel measurements at 304 GHz inside a train were presented in [15], and the key channel parameters, e.g., path loss, delay spread, and  $K$ -factor, were also presented. Furthermore, a ray-tracing method were proposed to simulate the intra-wagon channel model and verified from the measurement results. A measurement-based path loss model in a lecture room at 305 GHz was proposed in [14].

TABLE I: Recent studies on sub-THz short- and long-range channel measurement.

Reference	Frequency (GHz)	Sounder type	Scenario	Distance (m)	Channel parameters
Short-range					
[7]	250 - 300	VNA	Lab	2.3	Power angle spectrum.
[12]	275 - 325	VNA	Office	1.8 - 2.9	$K$ -factors, delay and angular spread.
[13]	300 - 308	Correlation	Office	4	Power angle spectrum.
[14]	300 - 310	VNA	Lecture room	2 - 5	Path loss
[15]	300 - 308	Correlation	Intrawagon	5.3	Path loss, delay and angular spread, polarization.
[16]	280 - 320	VNA	Data center	1.8	Path loss, shadowing, cluster number and power.
[17]	126 - 156	VNA	Lab, office, conference room	1.8 - 10.6	Path loss, delay spread, angular spread, cluster.
[18]	130 - 143	VNA	Meeting room	1.4 - 8.0	Path loss, delay and angular spread, cluster.
Long-range					
[19]	141.1 - 145.1	VNA with RoF	Shopping mall	3 - 65	Path loss, delay and angular spread.
[20]	141 - 148.5	VNA with RoF	Outdoor urban	104	Path loss, angular spread, cluster spread.
[21]	141 - 148.5	VNA with RoF	Outdoor urban	15.9 - 34.2	Path loss, angular spread.
[22]	141.5 - 142.5	Correlation	Whole office floor	3.9 - 39.2	Path loss, number, delays, and powers of clusters.
[23]	142	Correlation	Outdoor urban	up to 117.4	Path loss, penetration loss through foliage.
[24]	299-301	VNA with RoF	Corridor	27 & 43	Power angle spectrum, delay spread, and angular spread.

Only a handful of long-range measurements were reported in the long-range scenarios and mainly at 140 GHz [19]–[23]. VNA-based channel measurements at mmWave (i.e., 28 GHz) and sub-THz (i.e., 140 GHz) frequency bands, were performed in [19]. The measurement scenario is a large shopping mall and the measurement distance ranges from 3-65 m. The multipath components, delay spreads, and angular spreads of 28 GHz and 140 GHz were found to be similar. In [20], [21], 145 GHz outdoor channel measurements of up to 100 m measured distances were conducted. In [23], channel measurements at 140 GHz are performed in an outdoor urban environment. Moreover, path loss model, as well as a model of the penetration loss through foliage are provided. In [24], a long-range VNA-based channel sounder based on the radio-over-fiber techniques was developed. Besides, the channel measurements based on this channel sounder in a corridor scenario and the analyses of power angle spectrum, delay spread, and angular spread were presented, which is only a simple validation of the proposed long-range sounder. Table I provides the summaries of the channel measurements and modeling at sub-THz frequency bands. Note that this list is by no means complete and it is included here only to demonstrate some recent progress in the state-of-the-art works.

However, there is a lack of experimental studies on channels in long-range scenarios at 300 GHz. The high fidelity of our long-range channel sounder has been validated in [24]. However, the channel characteristics and channel models at 300 GHz are not further analyzed in [24] since the measured data were only collected at one measurement location. Therefore, in this study, channel measurements have been conducted using a double-directional scanning scheme (DDSS) to explore 300 GHz channel characteristics in a large hall scenario. Channel measurements are conducted with 8 different Transmitter (Tx)-Receiver (Rx) distance ranging from 3-15.6 m. Based on the large amount of the directional measurement data, i.e., 33120 channel frequency response (CFR), we calculate and analyze the power-angle-delay profiles (PADPs) and power-angle spectra (PAS). We also calculate and analyze key channel parameters including path loss, and dispersion spread in delay and angle domain.

The novelties of this study are outlined in the following

aspects:

- 1) Channel measurements are conducted at 300 GHz in a large hall scenario with the Tx-Rx distance range of 3-15.6 m.
- 2) We calculate and analyze the key measurement-based channel characteristics, i.e., PAS, PADP, path loss, delay and angular spread, in the LoS and NLoS cases. We also plotted the ray trajectories for the considered measurement locations.

The reminder of this paper is organized as follows. Section II illustrates the VNA-based sounder structure and the description of the measurement scenario. Section III gives the signal model and key channel parameters. Section IV highlights the results of this 300 GHz channel measurements. Conclusion are finally drawn in Section V.

## II. CHANNEL SOUNDER DEVELOPMENT AND MEASUREMENT SCENARIO

### A. Channel Sounder Development

Fig.1 and Table II depict the structure of the 300 GHz VNA-based sounder with RoF schemes and the components employed in the sounder, respectively. This channel sounder consists of two parts, i.e., VNA-based sounding system and RoF scheme. In the first part, we used a four-port VNA from Keysight (N5227B) and frequency extenders from VDI Inc. (VDI WR3.4). An radio frequency (RF) signal at 12.22-18.33 GHz is sent from the VNA to the Tx extender. In the Tx extender, the RF signal then passes through a multiplier with a factor of 18 and is converted to 220-330 GHz. A coupler is used to split the sub-THz signal, one of the split signals is used for transmission over the channel which needs to be measured. Note that the other split signal is demodulated to a 7.438 MHz signal and sent back to VNA for reference. The VNA also sends a local-oscillator (LO) signal at 9.12-13.75 GHz. The LO signal is then split into two signals by a power splitter and sent to the LO port in the Tx and Rx extenders. The LO signals are multiplied by a factor of 24 to demodulate the sub-THz signals. Finally, the 7.438 MHz reference signal and the demodulated received signal is sent to Port A and Port B, respectively.

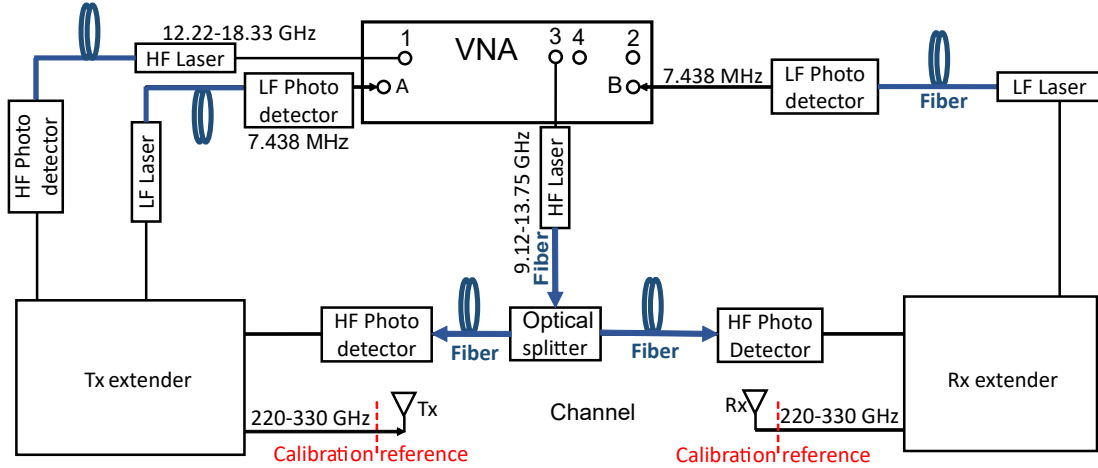


Fig. 1: Schematic diagram of the channel sounder using the RoF techniques.

The dynamic range of this sounder is limited due to the high power loss through the coaxial cables, thus constraining the measurement distance of this channel sounder. Therefore, we develop an RoF extension scheme in this work. The main idea is to raise the dynamic range and extend the measurement range using optical fiber cable which has a negligible signal loss (i.e., 0.8 dB/km). In the RoF system part, two RoF system working at two different frequency bands, i.e., high frequency (HF) for 0-50 GHz and low frequency (LF) for 0-6 GHz, are utilized. By using an electric-optical modulator, i.e., laser, the electrical signal is modulated to optical signal with the wavelength of 1550 nm. The optical signal is transmitted through an 300 m optical fiber cable and demodulated into an electrical signal. In principle this long-range channel sounder could reach to 600 m Tx-Rx separation. However, the measurement range might be limited by the measurement scenario in practice. In practical measurements, we must also consider over-the-air free space propagation loss and antenna misalignment loss (e.g., antenna alignment and polarization alignment).

To combat the high path loss, highly directive antennas are used in sub-THz channel measurements. In this work, the antenna gain for both sides is 26 dBi. The measured antenna pattern at 300 GHz is depicted in Fig. 2. The radiation pattern measurements were conducted in the anechoic chamber in Aalborg University, with a measurement distance of 9 m (i.e., direct far-field setup). Dynamic range is 50 dB in these measurements with the intermediate frequency bandwidth (IFBW) of 1 kHz. If we decrease IFBW to 10 Hz, we could get a higher dynamic range of 70 dB, however, the measurement time will explode. The measured half-power beamwidths (HPBW) in the H-plane and E-plane are  $8^\circ$  and  $6^\circ$ , respectively. Higher sidelobes is observed in the E-plane and the sidelobe level is seen to be  $-7.7$  dB. Note that only vertically polarized channels are investigated in this study.

### B. Measurement Scenario

Fig. 3 illustrates the measurement deployment. These channel measurements are carried out in a large hall with a size of  $42 \times 25$  m<sup>2</sup>. Note that the size of the corridor in this scenario is

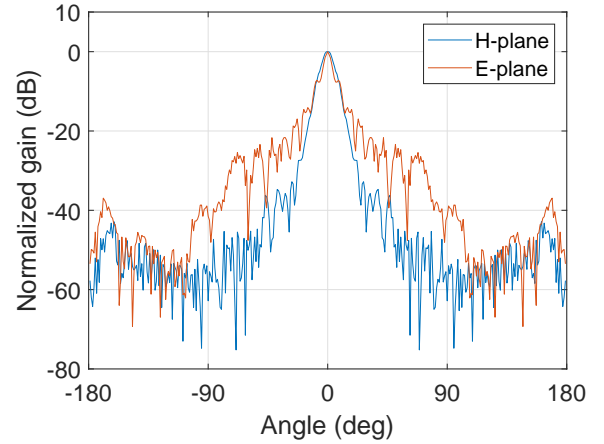


Fig. 2: Measured radiation pattern of the 300 GHz antenna.

TABLE II: Components for the channel sounder

Component	Type	Frequency/wavelength
VNA	Keysight N5227B	0.01-67 GHz
Frequency extender	VDI WR 3.4	220-330 GHz
HF laser	QMOD XMTQ-C-A-24	0 - 50 GHz
HF photo detector	QMOD XMRQ-C-A-24	0 - 50 GHz
LF laser	RFOF6T3FR-PA-11	0 - 6 GHz
LF photo detector	RFOF6R3FR-PA-11	0 - 6 GHz
Optical splitter	JDS FFC-CKH12B105-003	1550 nm

$43.4 \times 3.7$  m<sup>2</sup>. Fig. 4 illustrates the pictures in the real scenario. In these measurements, the Tx is deployed near the wall to mimic the base station, while four Rx measurement points are deployed to investigate the NLoS scenarios, (i.e., Rx 2 and Rx 4) as well LoS scenario (i.e Rx 1 and Rx 3). Note that Rx 4 is under the stairs and the LoS is completely blocked, while the NLoS case of Tx-Rx 2 is created by adding a metallic plate with the dimension of  $56 \times 85$  mm<sup>2</sup>, as depicted in Fig. 4 (a) and (c). Besides, we also conduct four channel measurements with different Tx-Rx distances in the LoS cases, i.e., Rx 5 - 8, to model the channel parameters.

To capture the channel information in the spatial domain, the DDSS was used in the measurements. Note that we performed

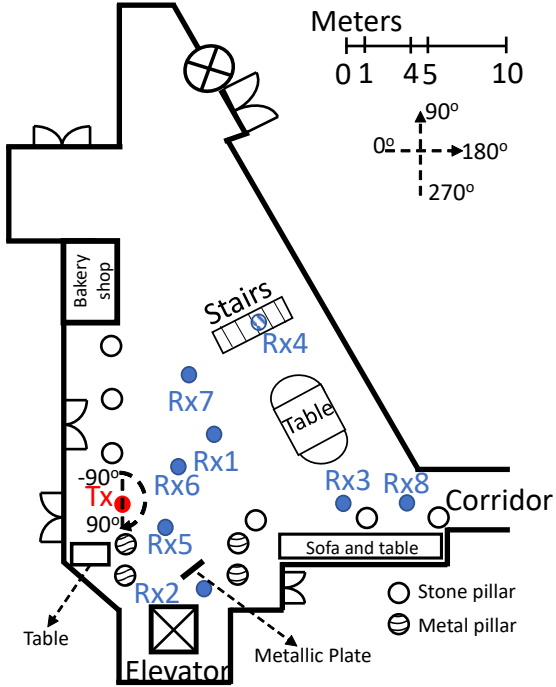


Fig. 3: Top view of the large hall scenario.

TABLE III: The measurement configuration in the large hall scenario.

Parameter	Value
Frequency range (GHz)	299-301
Bandwidth (GHz)	2
Frequency point	2001
Maximum detecting distance (m)	300
IFBW (kHz)	2
Transmitted power (dBm)	10
Antenna height (m)	1.25
LoS Tx-Rx distance (m)	5.9 (Rx 1), 11.4 (Rx 3)
NLoS Tx-Rx distance (m)	6.2 (Rx 2), 12 (Rx 4)
Tx-Rx distance for characterization (m)	3 (Rx 5), 4.2 (Rx 6)
Tx-Rx distance for characterization (m)	8.1 (Rx 7), 15.6 (Rx 8)
Tx azimuth rotation range (deg.)	$[-90, 90]$
Rx azimuth rotation range (deg.)	$[-180, 179]$
Rotation step (deg.)	4

an **over-the-air (OTA)** calibration to eliminate the effect of the system, **which uses 1 m LoS channel measurement results as a reference to calibrate the system and antenna response**. The picture of the channel sounder incorporated with the turntables is depicted in Fig. 5. As shown in Fig. 5, we mounted the Tx and the Rx extenders to two turntables. The Tx and the Rx are programmed to rotate the azimuth in the range of  $[-90^\circ, 90^\circ]$  and  $[-180^\circ, 176^\circ]$ , respectively. The rotation step is set to be  $4^\circ$  at both sides. According to [25], the  $4^\circ$  rotation angle step is sufficient for wideband channel spatial profile reconstruction. Thus, the number of channel frequency responses we obtained for each measurement point is  $45 \times 90 = 4140$ . In total, we obtained 33120 CFR (i.e., number of Tx-Rx pairs  $\times$  number of measurement locations). The detailed measurement specifications are demonstrated in Table III.

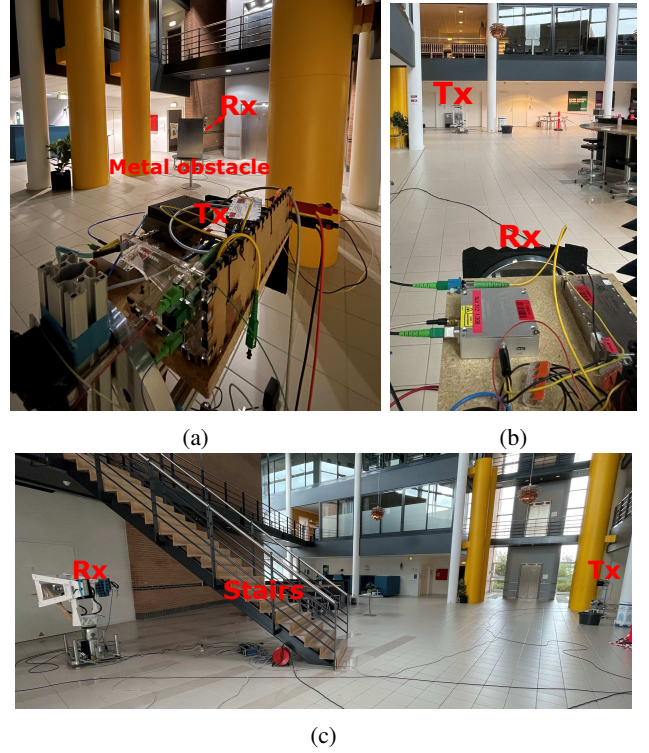


Fig. 4: Photos of the measurement scenario. (a) Tx-Rx 2; (b) Tx-Rx 3; (c) Tx-Rx 4.

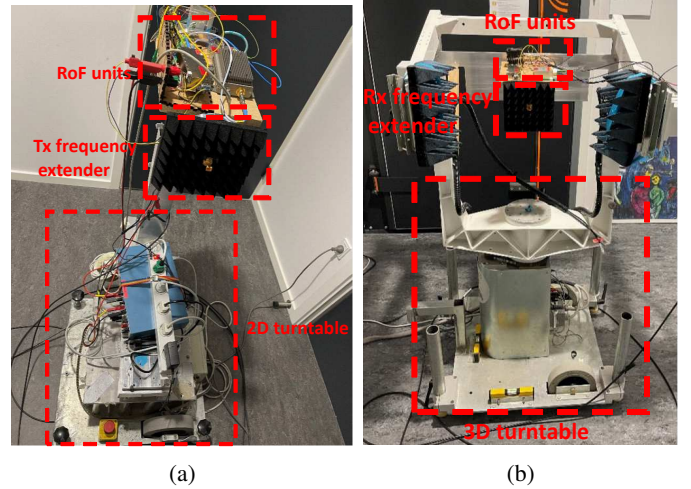


Fig. 5: Photos of the channel sounder mounted on the turntables. (a) Tx side; (b) Rx side.

### III. CHANNEL PARAMETER CHARACTERIZATION

#### A. Signal Model

The double-directional channel impulse response (CIR)  $h(\tau)$  in this work is written as:

$$h(\tau, \phi_{AoD}, \phi_{AoA}) = \sum_{\ell=1}^L \alpha_{\ell} \delta(\tau - \tau_{\ell}) \delta(\phi - \phi_{AoD, \ell}) \cdot \delta(\phi - \phi_{AoA, \ell}), \quad (1)$$

where  $\alpha_{\ell}$  and  $\tau_{\ell}$  denote the complex amplitude and the delay of the  $\ell$ th propagation path, respectively.  $\phi_{AoD, \ell}$  and

$\phi_{AoA,\ell}$  represent the angle-of-departure (AoD) and the angle-of-arrival (AoA) the  $\ell$ th path. And  $L$  represents the total number of propagation paths.

### B. DDPAS

From the measurements, we obtain the radio CFR  $H(f, \phi_{AoD}, \phi_{AoA})$ . The power delay profiles  $h(\tau, \phi_{AoD}, \phi_{AoA})$  can be obtained using inverse fast Fourier transform (IFFT), where  $f$ ,  $\tau$ ,  $\phi_{AoD}$ , and  $\phi_{AoA}$  denote the frequency, delay, AoD, and AoA, respectively.

The double-directional PAS (DDPAS)  $P(\phi_{AoD}, \phi_{AoA})$  can show the power distribution of the measured channel as a function of AoD  $\phi_{AoD}$  and AoA  $\phi_{AoA}$ . The DDPAS is calculated as:

$$P(\phi_{AoD}, \phi_{AoA}) = \sum_{\tau} |h(\tau, \phi_{AoD}, \phi_{AoA})|^2 \quad (2)$$

Note that in this paper, 10 dB higher than the noise floor is chosen to be the signal threshold for both LoS and NLoS cases.

### C. Omnidirectional PDP

In this paper, we analyze the omnidirectional power delay profile (PDP) by reconstructing the omnidirectional pattern from the full bidirectional capture. In this approach, we choose the direction with the highest power in each delay, similar to [26]:

$$P_{\text{omni}}(\tau) = \max_{\phi_{AoD}} \max_{\phi_{AoA}} |h(\tau, \phi_{AoD}, \phi_{AoA})|^2 \quad (3)$$

### D. Path loss

Path loss is a channel parameter that characterizes the power of the received signal as a function of distance. In this paper, path loss is calculated as the power summation of the omnidirectional PDP:

$$PL = \sum_{\tau} P_{\text{omni}}(\tau) \quad (4)$$

We fit the empirical path loss by two log-distance dependent path loss model, *i.e.*, alpha-beta-gamma (ABG) model and close in (CI) model, which is widely used in [27]–[29]. The ABG model can be written as:

$$PL_{ABG}(d)[\text{dB}] = 10n_{ABG} \log_{10}\left(\frac{d}{d_0}\right) + PL(d_0) + \chi_{\sigma}^{ABG} \quad (5)$$

where  $PL_{ABG}(d)$  (in dB) denotes the ABG path loss model over distance.  $d$  (in meter) represents the Tx-Rx distance with  $d \geq 1$  m and  $d_0 = 1$  m;  $n_{ABG}$  and  $PL(d_0)$  are the path loss exponent and the optimized offset value for path loss, respectively.  $\chi_{\sigma}^{ABG}$  represents the large-scale signal fluctuations.

The CI model is given as:

$$PL_{CI}(d)[\text{dB}] = 20 \log_{10}\left(\frac{4\pi f_c}{c}\right) + 10n_{CI} \log_{10}(d) + \chi_{\sigma}^{CI} \\ = 10n_{CI} \log_{10}(d) + 81.98 + \chi_{\sigma}^{CI} \quad (6)$$

where  $PL_{CI}(d)$  (in dB) denotes the CI path loss model over distance.  $n_{CI}$  and  $\chi_{\sigma}^{CI}$  are the path loss exponent and the large-scale signal fluctuations, respectively.

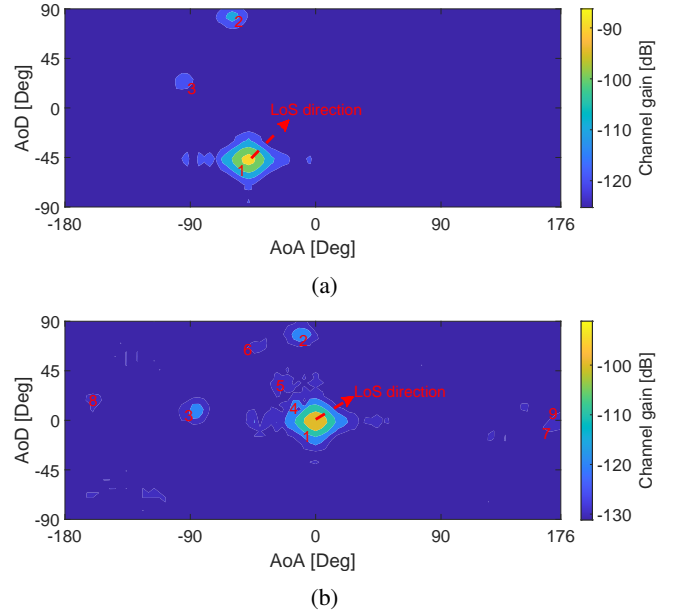


Fig. 6: Exemplary DDPAS for the LoS measurement locations. (a) Tx-Rx 1 (LoS); (b) Tx-Rx 3 (LoS).

### E. Delay Spread

Delay spread is a channel parameter that describes the delay span of the channel path. Note that we compute and analyze the delay spread based on the omnidirectional PDP  $P_{\text{omni}}(\tau)$ . In this study, the root-mean-square (RMS) delay spread of the channel  $\tau_{\text{rms}}$  is computed as

$$\tau_{\text{rms}} = \sqrt{\frac{\sum_{\tau} (\tau - \bar{\tau})^2 P_{\text{omni}}(\tau) d\tau}{\sum_{\tau} P_{\text{omni}}(\tau) d\tau}}, \quad (7)$$

where  $\tau_{\text{max}}$  is the maximum delay, *i.e.*, 750 ns, and  $\bar{\tau}$  is the average delay spread that is calculated as

$$\bar{\tau} = \frac{\sum_{\tau} \tau P_{\text{omni}}(\tau) d\tau}{\sum_{\tau} P_{\text{omni}}(\tau) d\tau} \quad (8)$$

### F. Angular Spread

In this study, angular spread is referred to as the AoD spread and the AoA spread denoted with  $\sigma_{\phi_{AoD}}$  and  $\sigma_{\phi_{AoA}}$ , respectively. In this work, the angular spread  $\sigma_{\phi}$  is calculated approximately as the second central-moment of the azimuth-power spectrum  $P(\phi)$ :

$$\sigma_{\phi} \approx \sqrt{\frac{\sum_{\phi} (\phi - \mu_{\phi})^2 \cdot P(\phi)}{\sum_{\phi} P(\phi)}}, \quad (9)$$

where  $\mu_{\phi}$  represent the mean angle, and it is calculated as,

$$\mu_{\phi} = \frac{\sum_{\phi} \phi \cdot P(\phi)}{\sum_{\phi} P(\phi)}. \quad (10)$$

## IV. MEASUREMENT RESULTS

In this section, channel parameters at 300 GHz are presented, including DDPAS, delay spread, angular spread, and path trajectory.

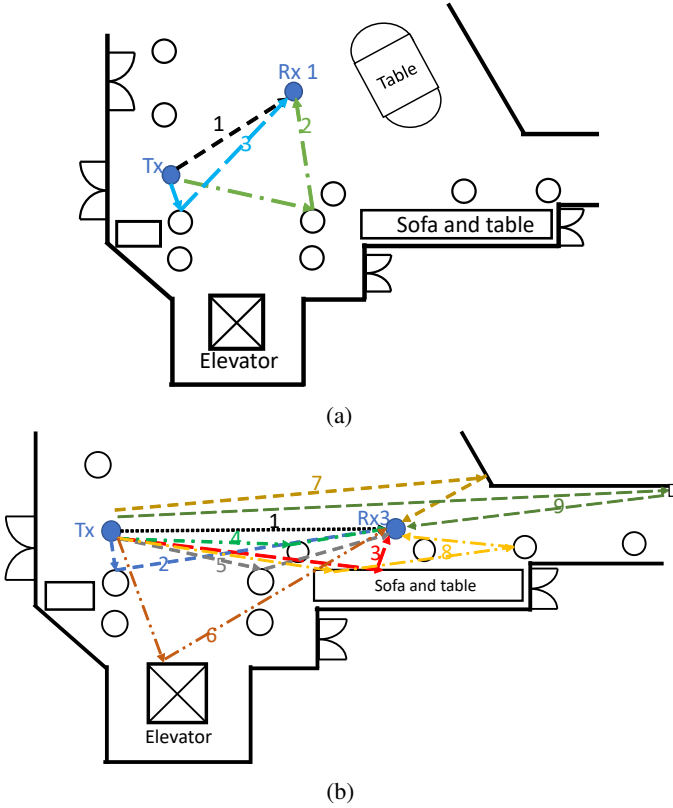


Fig. 7: Relationship between the main paths and the room geometry. (a) Tx-Rx 1;(b) Tx-Rx 3.

#### A. DDPAS

Fig. 6 and Fig. 9 (a) and (c) depict the exemplary DDPASs  $P(\phi_{Tx}, \phi_{Rx})$  and the PADPs of the measured LoS channel, respectively. Note that we use 40 dB threshold from the peak power value in the spectra, and the gain of the horn antenna has not been removed in the results. In the Tx-Rx 1 scenario, the LoS path has the delay of 20 ns, the AoD of  $-46^\circ$ , and the AoA of  $-48^\circ$ , which matches the geometry of the transceiver deployment. While the LoS component in the Tx-Rx 3 LoS scenario has the delay of 38 ns, the AoD of  $0^\circ$ , and the AoA of  $0^\circ$ . The power is observed to be highly concentrated around the LoS direction, while several additional reflection contributions from various directions are identified. Besides, the LoS path power decreases from  $-40.4$  dB to  $-45.3$  dB with the measurement distance increasing from 5.9 m to 11.4 m. The number of multipath components (MPCs) in these two LoS scenarios are seen to be 2 and 8, respectively. Note that path 9 is found to be the reflection from the window structure of the corridor. **The multipath is shown to be specular and sparse from the measured results.** Furthermore, Fig. 7 depicts the relation of the main paths in the channel to the room geometry, the delays, AoDs, AoAs of the main paths in the LoS scenarios match the room geometry.

The DDPAS and PADP in the Tx-Rx 2 NLoS scenario are depicted in Fig. 8 (a) and Fig. 9 (b), respectively. The LoS path can still be observed with the delay of 21 ns (which matches the Tx-Rx 2 distance of 6.2 m) and power of  $-77.2$  dB, which to our postulation, is due to the diffraction from the edge of

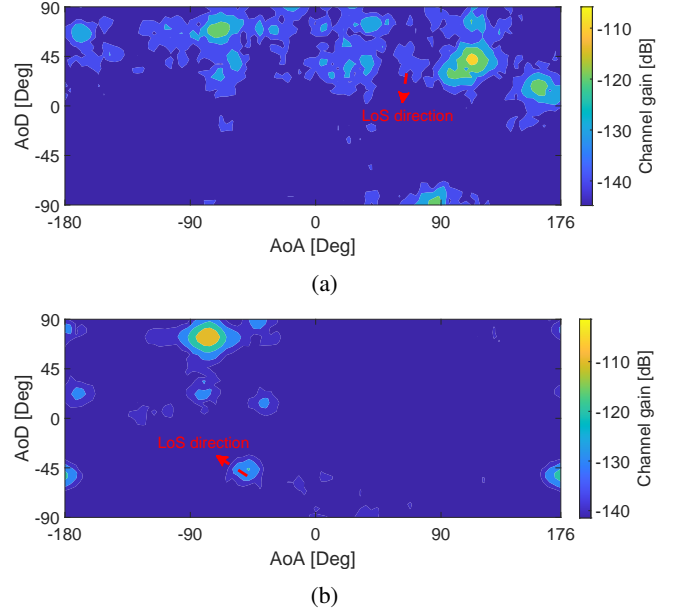


Fig. 8: DDPAS for the NLoS measurement locations. (a) Tx-Rx 2;(b) Tx-Rx 4.

the metal obstacle. Besides, the MPCs are mainly concentrated in the AoD range of  $[0^\circ, 90^\circ]$ . In the Tx-Rx 4 NLoS scenario, the LoS path is observed to be totally blocked by the stairs, and the MPCs in this case are mainly concentrated in the AoA range of  $[-180^\circ, 0^\circ]$ , as illustrated in Fig. 8 (b) and Fig. 9 (d). Furthermore, compared with the DDPAS from the LoS scenario in Fig. 6, the MPCs in the NLoS cases are richer compared to those in the LoS cases due to the fact that the dominant LoS components are blocked and thus, the difference in power between various MPCs is less.

#### B. Omnidirectional PDP and Path loss

Fig. 10 illustrates an exemplary omnidirectional PDP comparison. In Fig. 10 (a) (Rx 1 and Rx 2 cases), we observe that the LoS path in the OLoS case is blocked and the power decreases from  $-40.4$  dB to  $-67.7$  dB compared to that in the LoS case. We observe that the MPCs are rich for both cases. The MPCs mainly appear in the delay range of  $[21, 250]$  ns (corresponding to the propagation distance range of  $[6.3, 75]$  m). Furthermore, several weak paths over 400 ns (corresponding to the propagation distance of 120 m) can still be identified in both cases. In Fig. 10 (b) (Rx 3 and Rx 4 cases), the LoS path in the NLoS case (i.e., Rx 4) is completely blocked and the power reduction is 58.5 dB compared to LoS case. The MPCs in NLoS case mainly appear in the delay range of  $[50.5, 270]$  ns (corresponding to the propagation distance range of  $[15, 81]$  m), while the omnidirectional PDP in the LoS case is seen to have a longer decay in the delay range of  $[37.5, 446.5]$  ns. Note that we also identify one reflection path from the wall at the end of the corridor with the power of  $-79.0$  dB and the delay of 353.5 ns.

Fig. 11 depicts the comparison of the empirical path loss and the modeled path loss. Note that the antenna gain is removed

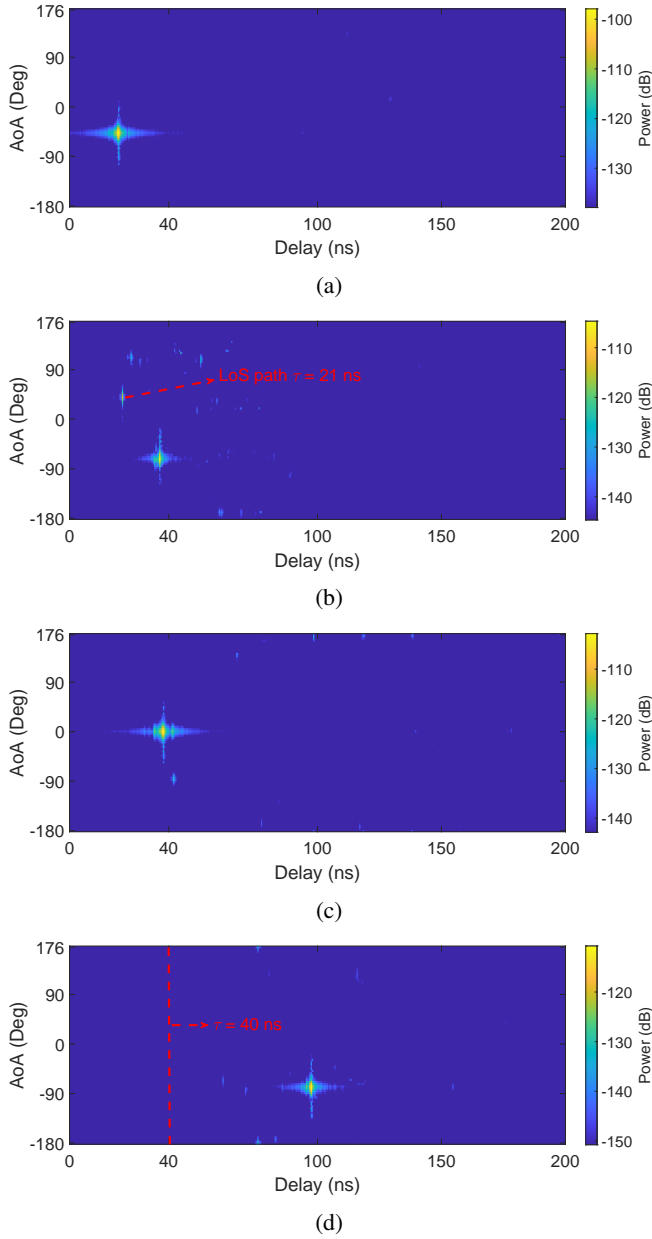


Fig. 9: Exemplary PADP for NLoS locations at the LoS direction. (a) Tx-Rx 1 ( $\phi_{Tx} = -46^\circ$ ); (b) Tx-Rx 2 ( $\phi_{Tx} = 50^\circ$ ); (c) Tx-Rx 3 ( $\phi_{Tx} = 0^\circ$ ); (d) Tx-Rx 4 ( $\phi_{Tx} = -50^\circ$ ).

from the omnidirectional PDP before the calculation. The empirical path loss in the NLoS scenarios is also illustrated in Fig. 10. The empirical path loss is well-fitted to the ABG path loss model of  $2.1 * 10 * \log_{10}(d) + 79.6$  with the root-mean-square error (RMSE) of 0.9 dB, and is also well-fitted to the CI model of  $1.8 * 10 * \log_{10}(d) + 82.0$  with the RMSE of 1.1 dB. The ABG model has higher accuracy compared to the CI model. We also compare the measured path loss with the free space path loss (FSPL) model. The fitted path loss exponent for ABG model  $n_{ABG} = 2.1$  matches the theoretical FSPL value. However, measured  $PL(d_0)$  is 1.6 dB less than the theoretical value due to the fact that the omnidirectional path loss is a wideband path loss. While the fitted exponent

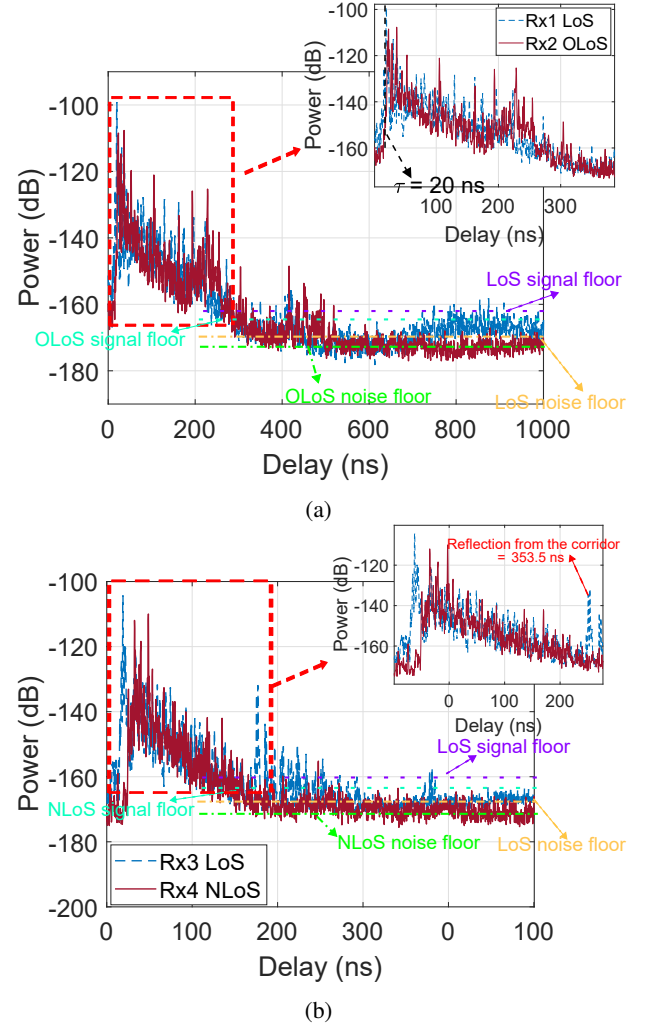


Fig. 10: Exemplary omnidirectional PDP comparison. (a) Rx 1 and Rx 2. (b) Rx 3 and Rx 4.

for CI model  $n_{CI} = 1.8$  is slightly lower than the theoretical value. Compared the NLoS path loss (i.e., Rx 2 and Rx 4) with the LoS path loss in the same Tx-Rx distance (i.e., Rx 1 and Rx 3), the path losses increase 3.3 dB and 4.7 dB, respectively.

### C. Delay spread

Fig. 12 depicts the comparison of the empirical delay spread. As illustrated in Fig. 12, the empirical delay spreads in the LoS cases range within [7.5, 35.6] ns. Besides, the LoS delay spreads increase with the link distance between the Tx and the Rx, which is due to the fact that as the LoS power decreases with the increasing distance, the power of MPCs becomes comparable to that of the LoS path. In the NLoS cases, the delay spread of the Rx 2 is 14.8 ns higher than that of Rx 1, while the delay spread of the Rx 4 is 7.6 ns lower than that of Rx 3. However, due to the lack of sufficient NLoS measurements, we cannot draw any conclusions for the NLoS delay spreads and further measurements should be carried out to investigate it.

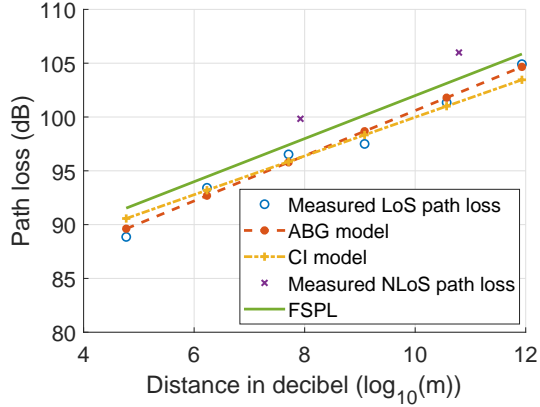


Fig. 11: Path loss models for these measurement results.

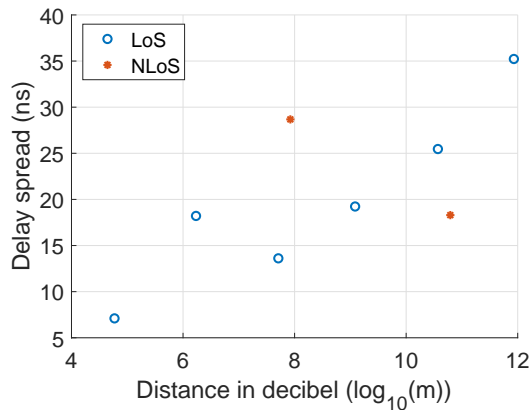
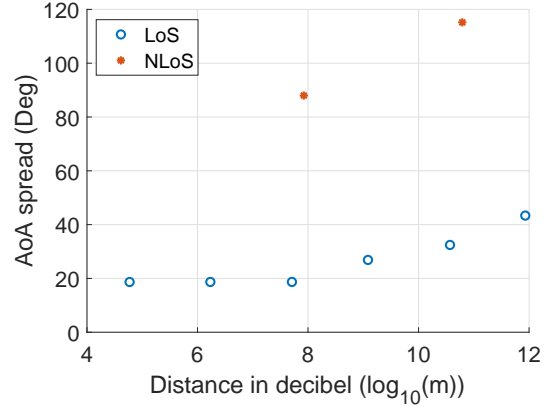


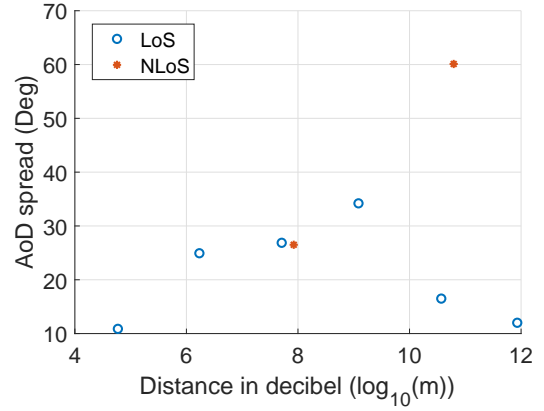
Fig. 12: Relation of the delay spread to the Tx-Rx distance.

#### D. Angular Spread

The relation of the empirical angular spread to the link distance between the Tx and Rx is depicted in Fig. 13. We observe that the LoS AoA spreads are ranging in  $[18^\circ, 43^\circ]$  and increases with the distance. Moreover, the LoS AoD spreads are seen to increase with the measurement distance range of  $[3, 8.1]$  m, and decrease in the Tx-Rx distance range of  $[8.1, 15.6]$  m. Fig. 14 illustrates the power-angle-spectrum (PAS) comparison of the Rx 3, Rx 7, and Rx 8. We observed that the Rx 7 has a larger AoD difference between the LoS direction and the mean AoD compared to those of the Rx 3 and Rx 8, which means that the MPCs contribute more to the angular spread in the Rx 7 case. For the NLoS scenarios, the AoA spreads of the two NLoS cases, i.e., Rx 2 and Rx 4, are  $88.0^\circ$  and  $115.2^\circ$ , respectively, which are observed to be much higher than those AoA spreads at the same distance. Fig. 15 illustrates the comparison of the PAS in azimuth and the mean azimuth in LoS and NLoS cases. It is observed that the mean AoA appears near the LoS peak in Rx 1 and Rx 3 (LoS cases), as shown in Fig. 15 (a), and the LoS power contributes dominantly to the angular spread, which leads to a small angular spread around the mean AoA (i.e., LoS) direction. Meanwhile, the LoS path is blocked in Rx 2 and Rx 4 (NLoS cases), and the MPCs and angle differences of



(a)



(b)

Fig. 13: Relation of the angular spread to the Tx-Rx distance. (a) AoA spread; (b) AoD spread.

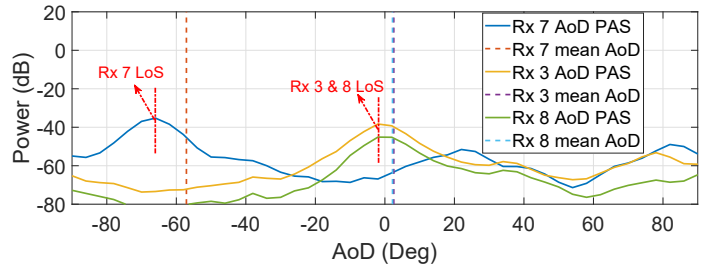


Fig. 14: The AoD PAS with the mean elevation and LoS direction.

the paths to the mean angle contributed more significantly to the angular spread. The AoD spread of the Rx 4 is  $43.6^\circ$  higher than that of Rx 3 and the AoD spread of the Rx 2 is found to be close to that of Rx 1.

#### E. Observation and Model Comparison to Existing Counterpart

- **The measured channels are seen to be specular and sparse.** The diffuse components are predicted to be more important in principle as the frequency goes up, since

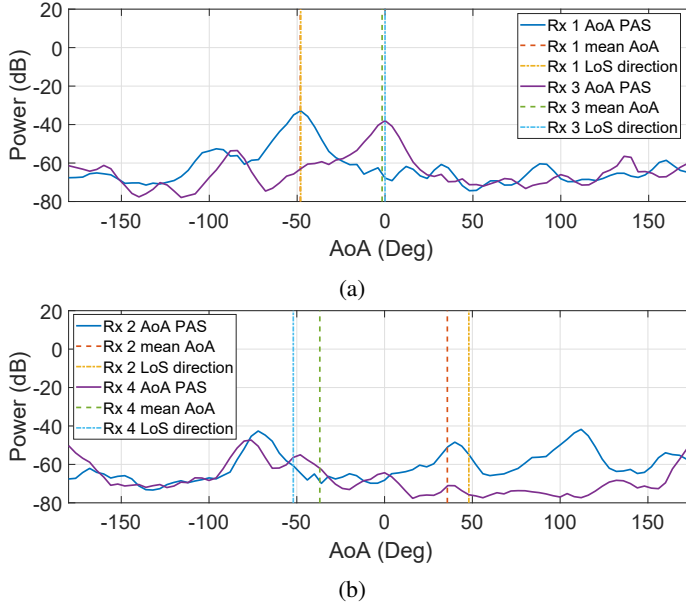


Fig. 15: The AoA PAS with the mean azimuth and LoS direction. (a) LoS cases. (b) NLoS cases.

the wavelength is getting close to the surface smoothness [30], [31]. However, this is not our observation here both for the LoS and NLoS scenarios, the measured channels are shown to be highly specular and sparse, due to its susceptibility to high transmission loss, blockage loss, and high diffraction loss. Furthermore, the wavelength at 300 GHz is around 1 mm, which is still much larger than the typical indoor surface roughness.

- In the 3GPP channel models, a channel modeling framework with cluster-level parameters is typically adopted for 3GPP SCME channel model and 3GPP 38.901 channel model. The measured data can provide realistic inputs on the channel parameter settings for the simulation.
- With respect to path loss, two widely-used log-distance path loss models are used and compared in this study. In the state-of-the-art, there are only a few literature reporting directional/double-directional channel models at 300 GHz frequency bands [15], [32], [33]. Table IV illustrates the comparison of the path loss model to the existing 300 GHz channel models. The fitted ABG model is found to be closed to that in [15] and the offset  $PL(d_0)$  in this study is seen to be 3.2 dB higher than that in [32]. The exponent of the fitted CI model is 0.4 higher than that in [33]. As for other parameters, the delay spread in this work is much higher than that in [15], [32], [33], which is due to the bigger scenario size and richer scatterer in our measurements. The AoA spread are observed to be close compared to those in [33] in the similar Tx-Rx distance.

## V. CONCLUSIONS

In this paper, we present the measurement results of the double-directional sub-THz channel measurements at 300 GHz bands in a large hall scenario. Firstly, we summarize the sub-THz channel measurements in the literature. A VNA-

based channel sounder using RoF scheme at 300 GHz is then proposed and channel measurements are performed in a large hall scenario. The Tx-Rx distances are from 3-15.6 m. We also consider LoS and NLoS cases in the measurements. Channel characteristics, *i.e.*, DDPAS, PADD, path loss, delay spread, and angular spread, are calculated and analyzed in the aforementioned scenario. The DDPAS results show a good agreement with the room geometry, which demonstrates the accuracy of the measurements. The DDPAS results in the LoS scenario also illustrates the sparsity of the multipaths at 300 GHz. The empirical path loss related to the measurement distance in decibel is well-fitted by the ABG model and found to be close to the theoretical FSPL model. The LoS delay spread is observed to increase with the Tx-Rx distance. Compared with the low angular spreads in the LoS cases, the angular spreads at NLoS cases are found to be much higher. Moreover, MPCs are observed in the omnidirectional PDP over 200 ns (which corresponds to 60 m). This result indicates the possibility of long-range channel measurement campaign at 300 GHz. Further long-range 300 GHz channel measurements should be conducted in the future.

## REFERENCES

- [1] T. S. Rappaport, Y. Xing, O. Kanhere, S. Ju, A. Madanayake, S. Mandal, A. Alkhateeb, and G. C. Trichopoulos, "Wireless communications and applications above 100 GHz: Opportunities and challenges for 6G and beyond," *IEEE Access*, vol. 7, pp. 78 729–78 757, 2019.
- [2] Z. Ma, B. Ai, R. He, Z. Zhong, and M. Yang, "A non-stationary geometry-based MIMO channel model for millimeter-wave UAV networks," *IEEE Journal on Selected Areas in Communications*, vol. 39, no. 10, pp. 2960–2974, 2021.
- [3] Z. Huang and X. Cheng, "A general 3D space-time-frequency non-stationary model for 6G channels," *IEEE Transactions on Wireless Communications*, vol. 20, no. 1, pp. 535–548, 2021.
- [4] A. Pärssinen, M.-S. Alouini, M. Berg, T. Kürner, P. Kyösti, M. E. Leinonen, M. Matinmikko-Blue, E. McCune, U. Pfeiffer, and P. Wambacq, "White paper on RF enabling 6G opportunities and challenges from technology to spectrum," *6G Flagship Ecosystem*, Apr. 2021. [Online]. Available: <https://www.6gchannel.com/items/6g-white-paper-rf-spectrum/>
- [5] T. Kürner and S. Priebe, "Towards THz communications - status in research, standardization and regulation," *Journal of infrared, millimeter and terahertz waves*, vol. 35, no. 1, pp. 53–62, 2014.
- [6] Y. Yuan, R. He, B. Ai, Z. Ma, Y. Miao, Y. Niu, J. Zhang, R. Chen, and Z. Zhong, "A 3D geometry-based THz channel model for 6G ultra massive MIMO systems," *IEEE Transactions on Vehicular Technology*, vol. 71, no. 3, pp. 2251–2266, 2022.
- [7] Y. Lyu, P. Kyösti, and W. Fan, "Sub-terahertz channel sounder: Review and future challenges," *China Communications*, 2022.
- [8] J. Zhang, P. Tang, L. Yu, T. Jiang, and L. Tian, "Channel measurements and models for 6G: current status and future outlook," *Frontiers of information technology & electronic engineering*, vol. 21, no. 1, pp. 39–61, 2020.
- [9] A. W. Mbugua, W. Fan, K. Olesen, X. Cai, and G. F. Pedersen, "Phase-compensated optical fiber-based ultrawideband channel sounder," *IEEE Transactions on Microwave Theory and Techniques*, vol. 68, no. 2, pp. 636–647, 2020.
- [10] J. Huang, C. Wang, R. Feng, J. Sun, W. Zhang, and Y. Yang, "Multi-frequency mmwave massive MIMO channel measurements and characterization for 5G wireless communication systems," *IEEE Journal on Selected Areas in Communications*, vol. 35, no. 7, pp. 1591–1605, 2017.
- [11] Y. Lyu, A. W. Mbugua, K. Olesen, P. Kysti, and W. Fan, "Design and validation of the phase-compensated long-range sub-thz vna-based channel sounder," *IEEE Antennas and Wireless Propagation Letters*, vol. 20, no. 12, pp. 2461–2465, 2021.
- [12] S. Priebe, M. Kannicht, M. Jacob, and T. Kürner, "Ultra broadband indoor channel measurements and calibrated ray tracing propagation modeling at THz frequencies," *Journal of Communications and Networks*, vol. 15, no. 6, pp. 547–558, 2013.

TABLE IV: The Comparison of Path Loss Models at 300 GHz bands.

Ref.	Frequency (GHz)	Conditions	Path loss model	Delay spread	AoA spread
Fitted model	299-301	Large hall, $3 \leq d \leq 15.6$ m	$PL_{ABG}(d) = 2.1 * 10 * \log_{10}(d) + 79.6$ $PL_{CI}(d) = 1.8 * 10 * \log_{10}(d) + 82.0$	[7.1, 35.2] ns	[18.7°, 43.4°]
[15]	300-308	Intra-wagon, $d = 5.3$ m	$PL_{ABG}(d) = 2.2 * 10 * \log_{10}(d) + 79.8$	[1.2, 2.6] ns	22.8°
[32]	270-300	Office room, $1 \leq d \leq 6.6$ m	$PL_{ABG}(d) = 1.9 * 10 * \log_{10}(d) + 82.8$	[2.3, 7.9] ns	-
[33]	306-321	Corridor, $7.7 \leq d \leq 18.5$ m	$PL_{CI}(d) = 1.4 * 10 * \log_{10}(d) + 82.4$	[10.19, 20.69] ns	[20.0°, 52.1°]

- [13] E. M. Vitucci, M. Zoli, F. Fuschini, M. Barbiroli, V. Degli-Esposti, K. Guan, B. Peng, and T. Kürner, "Tri-band mm-wave directional channel measurements in indoor environment," in *2018 IEEE 29th Annual International Symposium on Personal, Indoor and Mobile Radio Communications (PIMRC)*, 2018, pp. 205–209.
- [14] Y. Zantah, F. Sheikh, A. A. Abbas, M. Alissa, and T. Kaiser, "Channel measurements in lecture room environment at 300 GHz," in *2019 Second International Workshop on Mobile Terahertz Systems (IWMTS)*, 2019, pp. 1–5.
- [15] K. Guan, B. Peng, D. He, J. M. Eckhardt, S. Rey, B. Ai, Z. Zhong, and T. Kürner, "Channel characterization for intra-wagon communication at 60 and 300 GHz bands," *IEEE Transactions on Vehicular Technology*, vol. 68, no. 6, pp. 5193–5207, 2019.
- [16] C. Cheng, S. Sangodoyin, and A. Zaji, "THz cluster-based modeling and propagation characterization in a data center environment," *IEEE Access*, vol. 8, pp. 56 544–56 558, 2020.
- [17] L. Pometcu and R. D'Errico, "An indoor channel model for high data-rate communications in D-band," *IEEE Access*, vol. 8, pp. 9420–9433, 2020.
- [18] Y. Chen, Y. Li, C. Han, Z. Yu, and G. Wang, "Channel measurement and ray-tracing-statistical hybrid modeling for low-terahertz indoor communications," *IEEE Transactions on Wireless Communications*, vol. 20, no. 12, pp. 8163–8176, 2021.
- [19] S. L. H. Nguyen, J. Irvellinen, A. Karttunen, K. Haneda, and J. Putkonen, "Comparing radio propagation channels between 28 and 140 GHz bands in a shopping mall," in *12th European Conference on Antennas and Propagation (EuCAP 2018)*, 2018, pp. 1–5.
- [20] N. A. Abbasi, A. Hariharan, A. M. Nair, A. S. Almainan, F. B. Rottenberg, A. E. Willner, and A. F. Molisch, "Double directional channel measurements for THz communications in an urban environment," in *ICC 2020 - 2020 IEEE International Conference on Communications (ICC)*, 2020, pp. 1–6.
- [21] N. A. Abbasi, J. Gomez-Ponce, S. M. Shaikbepari, S. Rao, R. Kondaveti, S. Abu-Surra, G. Xu, C. Zhang, and A. F. Molisch, "Ultra-wideband double directional channel measurements for THz communications in urban environments," in *ICC 2021 - IEEE International Conference on Communications*, 2021, pp. 1–6.
- [22] S. Ju, Y. Xing, O. Kanhere, and T. S. Rappaport, "Millimeter wave and sub-terahertz spatial statistical channel model for an indoor office building," *IEEE Journal on Selected Areas in Communications*, vol. 39, no. 6, pp. 1561–1575, 2021.
- [23] Y. Xing and T. S. Rappaport, "Propagation measurements and path loss models for sub-THz in urban microcells," in *ICC 2021 - IEEE International Conference on Communications*, 2021, pp. 1–6.
- [24] M. Bengtson, Y. Lyu, and W. Fan, "Long-range vna-based channel sounder: Design and measurement validation at mmwave and sub-thz frequency bands," *China Communications*, Aug. 2022.
- [25] W. Fan, F. Zhang, Z. Wang, O. K. Jensen, and G. F. Pedersen, "On angular sampling intervals for reconstructing wideband channel spatial profiles in directional scanning measurements," *IEEE Transactions on Vehicular Technology*, vol. 69, no. 11, pp. 13910–13915, 2020.
- [26] S. Hur, Y. J. Cho, J. Lee, N. G. Kang, J. Park, and H. Benn, "Synchronous channel sounder using horn antenna and indoor measurements on 28 GHz," in *2014 IEEE International Black Sea Conference on Communications and Networking (BlackSeaCom)*, 2014, pp. 83–87.
- [27] T. S. Rappaport, G. R. MacCartney, M. K. Samimi, and S. Sun, "Wideband millimeter-wave propagation measurements and channel models for future wireless communication system design," *IEEE Transactions on Communications*, vol. 63, no. 9, pp. 3029–3056, 2015.
- [28] S. Sun, T. S. Rappaport, S. Rangan, T. A. Thomas, A. Ghosh, I. Z. Kovacs, I. Rodriguez, O. Koymen, A. Partyka, and J. Jarvelainen, "Propagation path loss models for 5G urban micro- and macro-cellular scenarios," pp. 1–6, 2016.
- [29] K. Haneda, N. Omaki, T. Imai, L. Raschkowski, M. Peter, and A. Roivainen, "Frequency-agile pathloss models for urban street-canyons," *IEEE Transactions on Antennas and Propagation*, vol. 64, no. 5, pp. 1941–1951, 2016.
- [30] V. Degli-Esposti, D. Guiducci, A. de'Marsi, P. Azzi, and F. Fuschini, "An advanced field prediction model including diffuse scattering," *IEEE Transactions on Antennas and Propagation*, vol. 52, no. 7, pp. 1717–1728, 2004.
- [31] "METIS channel models," document Deliverable/ICT-317669/D1.4 V3, Tech. Rep., Mar. 2017.
- [32] M. Lotti, M. Caillet, and R. D'Errico, "Comparison of indoor channel characteristics for sub-THz bands from 125 GHz to 300 GHz," in *2022 16th European Conference on Antennas and Propagation (EuCAP)*, 2022, pp. 1–5.
- [33] Y. Wang, Y. Li, Y. Chen, Z. Yu, and C. Han, "0.3 THz channel measurement and analysis in an l-shaped indoor hallway," in *ICC 2022 - IEEE International Conference on Communications*, 2022, pp. 2870–2875.